Bora wind in Slovenia

Maruška Mole

Supervisors: Prof. Dr. Samo Stanič, Asst. Prof. Dr. Klemen Bergant

Graduate Physics Seminar

University of Nova Gorica

Abstract

A phenomenon of strong, gusty, downslope wind, where the cold air flowing over an orographic barrier sinks and accelerates as it encounters warm air at the lee side is generally referred to as Bora wind. The seminar provides an overview of Bora wind effects, synoptic situations that lead to its occurrence, classification of Bora wind events and mathematical formalism of airmass motion needed for its analytic description. In its second part, we focus on experimental devices and techniques applicable to the wind field measurements, in particular in-situ measurements using anemometers and remote sensing measurements using lidars. In its final part we present a case study of Bora wind events in Vipava valley in period from January to April 2012, its preliminary results and the prospect for future research.

Contents

1 Bora wind in Slovenia

Bora wind is a phenomenon well known in south-west (SW) part of Slovenia as well as along the Croatian coast line, where it reaches its peak magnitudes around the town of Senj (Fig. 1). Duration and frequency of Bora events in general decrease from the north to the south of Adriatic. Winds similar to Bora are known all around the world, from Japan to Greenland and Mexico, their common characteristic being the flow of cold air-masses over an orographic barrier.

Figure 1: Regions along Adriatic coast affected by Bora wind. 1 – Karst, 2 – Velebit [1].

In Slovenia, Bora wind occurs when cold air-masses move over the Eastern Alps. The cold air flows over two cols – Strmec and Postojna – and down the slopes into the SW Slovenia. Bora is more frequent in the winter time and can reach speeds up to 52 m/s in Vipava valley [2]. A good indicator of the lee-side wind speed is typically a cross-mountain pressure gradient [3].

Figure 2: The effects of the Bora wind – bent trees (left) [4], truck turned over due to the strong wind (center) [5], the uncovered roof (right) [6].

Strong winds affect many different aspects of life in the regions where they occur. Just a look around the landscape shows some of its effects – prevailing wind direction causes the deformation of trees, which are bent in the wind direction. Strong winds cause

many problems in agriculture as they blow away the fertile soil and take away most of the moist. As a result, dry land is more prone to wildfires, which are in addition hard to control due to the wind. Strong winds affect the traffic as well as the gusts may be strong enough to move smaller vehicles and turn over the bigger ones. In the case of strong Bora wind events in the Vipava valley the roads are closed for trucks and the maximum speed of the other vehicles is limited. The winds can cause snowdrifts on railways and roads. Sea traffic is affected as well, as most of the ships need to stay in the docks. The buildings in the Bora region have to be built to withstand its gusts – one can notice stones on the roof tops of older houses, the roofs have no overhangs and the taller objects (such as electric and telephone cables, road signs) have to be adequately fixed not to get knocked down by the wind.

The prediction of possible strong Bora wind outbursts is very important to prevent traffic problems and economic losses. The main problem of Bora wind prediction in general is poor knowledge of the mechanisms which lead to strong or extremely strong Bora events. The investigation of the conditions leading to such events by traditional measuring methods can not give the resolution needed to understand the problem in detail. However, the use of remote sensing systems such as rapid scanning elastic lidar could offer better overview of the 3-dimensional (3D) structure of the wind field and the processes taking place on the scale of a few meters, where the turbulence leading to strong wind gusts is most prominent.

1.1   Analysis and measurements of Bora wind in Slovenia

Many studies on the Bora wind in Slovenia already exist, where one of the first was made by Paradiž in 1957 [7]. Paradiž explained the connection between synoptic situation and occurrence of strong winds as well as the basic mechanism of strong wind development. The colder air flowing from the north-east (NE) over the orographic barrier encounters the warm air on the lee side of the barrier, sinks down and accelerates, converting its potential energy into kinetic energy.

Long lasting Bora wind events require the presence of a cyclone in the Northern (N) Mediterranean, which ensures constant flow of warm air from the SW. The incoming airmass is much colder than the airmass on the lee side of the mountain barrier ensuring the colder air falls over the barrier and accelerates due to the temperature difference. Cold air warms up adiabatically, which means the temperature difference to warm air is getting smaller (temperature gradient of warm, stably stratified air is smaller than adiabatic). In certain cases the air flowing from NE is not cold enough to reach the bottom of the valley just due to the temperature difference, and is forced down due to already existing flow. The resulting foehn wind is warm and very dry, reaching lower speeds than Bora.

1.1.1   Classification of Bora wind events

Some authors separate Bora events into two categories – cyclonic and anticyclonic Bora. The first occur in SW Slovenia due to the existing low pressure system in south (S) Adriatic region. The weather conditions in the case of cyclonic Bora are cloudy, with some rainfall due to warm air flowing over the cold airmass. Wind speeds in such a case

are uniform. In the case of anticyclonic Bora the sky is clear, the clouds appear only at the top of mountain barriers. Anticyclonic Bora is strong, but more localized. The prevailing synoptic situation in this case is strong anticyclone over NE Europe.

Paradiž points out such classification is not precise enough [7]. Measurements show that Bora wind is not the strongest in the case of anticyclone presence over NE Europe as it would be expected from the above mentioned classification. He explains the wind is usually a direct consequence of pressure differences due to synoptic systems. In regions of Bora wind appearance, the temperature difference between cold and warm air exists due to cold air being trapped behind the mountain barrier, causing pressure difference as well. Considering two possible reasons for the pressure gradient, he proposes 4 different cases of Bora events:

1. *The trapped air Bora (**T**)*: There is almost no pressure gradient due to synoptic events, the pressure difference between central and SW Slovenia exists purely due to temperature differences between cold air trapped behind the barrier and warm air on the other side. The Bora wind occurs due to the flow of cold air over barrier and is strongest near to the barrier. This type of Bora usually occurs momentarily, wind speed changes from zero to maximum value in a very short time.

2. *The trapped air and pressure gradient Bora (**T-G**)*: The pressure gradient already exist due to anticyclone over NE Europe, which maintains the temperature of the cold airmass behind the barrier, while the SW Slovenia is under the influence of cyclone in the S Adriatic region, which ensures the flow of warm airmass to the area on the other side of the barrier. Winds are strongest right under the barrier in this case and Bora event can last for few days if the cyclone persists.

3. *The pressure gradient and trapped air Bora (**G-T**)*: The temperature difference between cold and warm air is smaller than in the previous case due to weaker anticyclonic system over NE Europe or/and weaker cyclonic system in S Adriatic. Wind speed is approximately constant in the cold air behind the barrier as well as in the lee side of mountain and the valley below.

4. *The pressure gradient Bora (**G**)*: The wind exists only due to the pressure difference and is much warmer, dryer and slower than usual Bora wind.

Similar classification for the whole N Adriatic region was made also by Yoshino [8] – he proposed 4 different cases as well, though his classification is based on synoptic situation:

1. *Anticyclonic Bora of type **Aa*** occurs, when NE Europe and E Adriatic are under influence of high pressure, while there's a ridge over British Isles and through over Balkans at 500 mbar, and a high at sea-level over N France.

2. *Anticyclonic Bora of type **Ab*** occurs, when the Western (W) Europe lies under a planetary trough and the high extends to central Europe.

3. *Cyclonic Bora of type **Ba*** occurs, when there is a col of high pressure over the Atlantic and another over the continental Europe and as well the low pressure over Mediterranean Sea and over Iceland at the sea-level, while there's a planetary through over W Mediterranean Sea at 500 mbar.
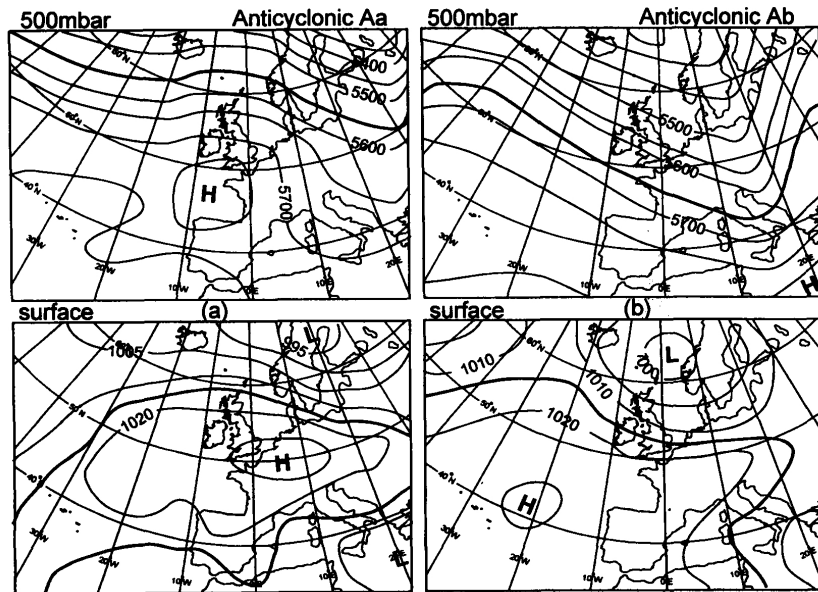
Figure 3: Synoptic charts for anticyclonic Bora **Aa** (left) and anticyclonic Bora **Ab** (right) at 500 mbar and sea-level [8].

4. *Cyclonic Bora of type **Bb*** occurs in similar conditions as the type **Ba**, but with more prominent low over W Mediterranean Sea and a high over the Atlantic.

Synoptic charts for all four cases are shown in Fig. 3 and 4. The types of Bora according
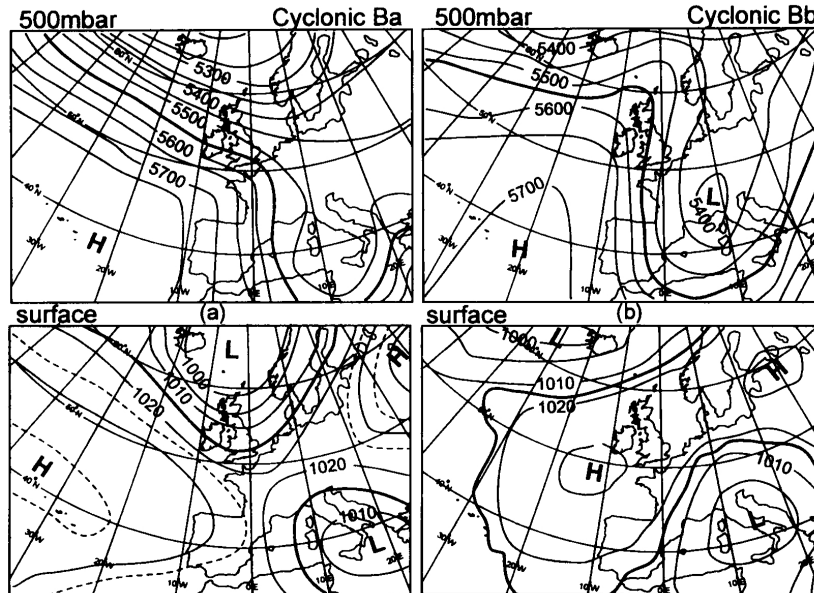

Figure 4: Synoptic charts for cyclonic Bora **Ba** (left) and cyclonic Bora **Bb** (right) at 500 mbar and sea-level [8].

to Paradiž and Yoshino can not be directly connected – in case of anticyclonic or cyclonic Bora the occurrence of more than one of the types Paradiž proposed can be observed. In the case of anticyclonic Bora of both types the occurrence of either **T-G** or **G-T** Bora

is possible in the beginning while at the end of the event even a weak **G** Bora can be observed.

1.1.2 Wind gusts

Bora wind is well known for its gustiness. First measurements provided basic information about its average speed, but not the maximum speed as the data given was an average speed over a short period of time (usually 5 to 10 minutes). First studies of the rate of occurrence, the duration period and daily distribution were made by Paradiž [7], and followed by studies of Paradiž and Petkovšek [10], who analyzed Bora at two measuring stations (Ajdovščina and Koper). The studies showed Bora wind is stronger in colder half of the year, where the occurrence of Bora is more frequent and the duration of a single event longer, while in summer time Bora is considerably weaker [2].

1.1.3 Wind direction

The wind rose diagrams of wind direction from the Bora region show the general direction of Bora wind is NE, though the direction may vary with respect to the terrain configuration. In some cases Bora wind can be confused with the land breeze as well, though both can usually be easily distinguished by the temperature difference in lower layers of atmosphere [11]. Land breeze is a wind driven by the temperature difference between land and sea, it occurs when the land is warmer than the sea. In the case of [11] the difference in temperature was estimated by the mean mixed layer potential temperature (MMLPT) obtained from radiosunding data from Zagreb and Udine, where Bora wind cases are the ones with higher values of MMLPT in Udine compared to Zagreb.

2 Downslope winds

The occurrence of Bora wind in SW Slovenia is a consequence of the stably stratified airmasses flowing from NE over the ridges of Trnovski gozd, Nanos and Javorniki plateaus to Vipava valley and Karst region. The flow of cold air down the slopes causes strong winds at the lee side of the barrier. The strongest gusts can be observed directly under the barriers. In general winds caused by the flow over the barrier are called downslope winds. They typically occur when stably stratified air is forced to rise over a topographic barrier. The topographic barrier causes the air to oscillate and form the so-called mountain waves, which can be classified as inner gravity waves. The direct consequence of such waves is a drag to the upper level of atmosphere, possible clear-air turbulence (CAT) and strong surface winds blowing down the lee side of the mountains.

2.1 Atmospheric stability

The downslope winds only occur if the atmosphere is stably stratifed. Atmospheric stability can be regarded as static or dynamic. Static stability is a measure of the buoyant convection of an air parcel, a small volume of air, which can differ from the surroundings in density, temperature and composition, but has the same pressure. The parcel of air moving upwards experiences cooling and expanding with the rate of cooling known as Dry Adiabatic Lapse Rate (DALR), which is $-9.8\,°C/km$. The observed Environmental Lapse Rate (ELR) can differ from the DALR value. If the atmosphere is statically stable (ELR > DALR), air parcel moving up will cool faster than the surrounding air, causing it to sink back to its original position (Fig. 5). When the atmosphere is statically neutral (ELR = DALR), the air parcel will cool with the same rate as the surrounding air, so the parcel will lift up to the position, where its vertical velocity will be 0 and stay there. When the atmosphere is statically unstable – convective (ELR < DALR), rising air parcel will cool slower than surrounding air, causing it to continue lifting up [12].

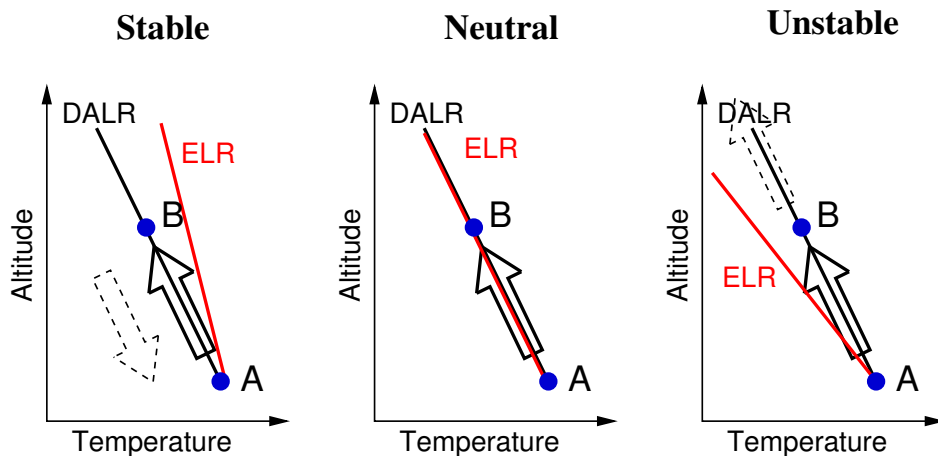Figure 5: The three classes of static stability – stable (ELR > DALR), neutral (ELR = DALR) and unstable (ELR < DALR).

Static stability is however not a good enough measure of the stability of the atmosphere. Take for example a statically stable layer of warm air overlying the layer of cold

air with strong winds. Even though the upper layer is stable at first, the wind shear across the interface causes laminar flow to become dynamically unstable. Dynamic stability is therefore the appropriate measure of the capability of the atmosphere to generate or suppress turbulence in the presence of strong winds.

2.2 Description of airmass motion

The state of an air parcel is described by a set of basic equations – continuity equation, equation of state or the ideal gas equation, equations of motion in x, y and z direction and thermodynamic equation. We can describe properties of the flow from a fixed reference frame (Eulerian picture of the flow) or from a reference frame moving with the flow (Lagrangian picture). The link between the two is the so called advective or material derivate:

$$\frac{\mathrm{D}}{\mathrm{D}t} = \frac{\partial}{\partial t} + \vec{u} \cdot \nabla,$$
(1)

which represents the rate of change with respect to time following the motion.

Continuity equation

Consider a fixed box, through which the fluid is moving. The rate of mass change within the box depends on the net mass flux into the box (Eulerian picture):

$$\frac{\partial \rho}{\partial t} + \nabla(\rho \vec{u}) = 0.$$

After using standard vector-calculus identity $\nabla(\rho \vec{u}) = \rho \nabla \cdot \vec{u} + \vec{u} \nabla \rho$ and recognizing the total derivate, we can rewrite the continuity equation as:

$$\frac{D\rho}{Dt} + \rho \nabla \vec{u} = 0,$$
(2)

which represents the rate of change of the volume of an air parcel with a fixed mass in time (Lagrangian picture).

Ideal gas equation

The state of gas is determined by basic atmospheric variables – pressure, temperature and density:

$$p = \rho RT = \frac{1}{\alpha} RT,$$

where R is the gas constant for dry air ($R = 287$ J/kgK).

Equations of motion

The motion of an airmass can be described by the Newton's second law for a fluid

$$(\rho \delta V)\vec{a} = \delta \vec{F},$$

where the forces influencing the motion are the pressure gradient force $\delta \vec{F}_{press} = -\delta V \nabla p$, the gravity force $\delta \vec{F}_{grav} = -g \delta V \hat{k}$ and the viscous force $\delta \vec{F}_{visc} = -\delta V \eta (\nabla^2 \vec{u} + \frac{1}{3} \nabla(\nabla \cdot \vec{u}))$.

Applying Newton's second law we derive Navier-Stokes or momentum equation for the compressible fluid flow in an inertial reference frame

$$\frac{Du}{Dt} = -\frac{1}{\rho}\nabla p - g\hat{k} + \vec{F}_{visc}. \tag{3}$$

The airmass is moving along with the Earth, so our reference frame is not inertial. In rotating reference frame we have to include the influence of the apparent forces – Coriolis and centripetal force:

$$\vec{a}_i = \vec{a}_r + 2\vec{\Omega} \times \vec{u}_r + \vec{\Omega} \times (\vec{\Omega} \times \vec{r}). \tag{4}$$

The Navier-Stokes equation in rotating reference frame is therefore

$$\frac{Du}{Dt} = -\frac{1}{\rho}\nabla p - g\hat{k} + \vec{F}_{visc} - 2\vec{\Omega} \times \vec{u}_r - \vec{\Omega} \times (\vec{\Omega} \times \vec{r}). \tag{5}$$

It is convenient to use spherical coordinate system (r, λ, ϕ) where r is the distance from the center of the Earth to the air parcel, λ is longitude and ϕ is latitude. At the surface, the unit vector $\hat{i}$ is pointing eastwards, $\hat{j}$ is pointing northwards and $\hat{k}$ upwards. Small displacements in each direction in spherical coordinate system can be written as

$$dx = r\cos\phi d\lambda,$$

$$dy = rd\phi,$$

$$dz = dr,$$

and the equations of motion in component form as:

$$\frac{Du}{Dt} - \frac{uv\tan\phi}{r} + \frac{uw}{r} = -\frac{1}{\rho}\frac{\partial p}{\partial x} + 2\Omega v\sin\phi - 2\Omega w\cos\phi + F_{rx}$$

$$\frac{Dv}{Dt} + \frac{u^2\tan\phi}{r} + \frac{vw}{r} = -\frac{1}{\rho}\frac{\partial p}{\partial y} - 2\Omega u\sin\phi + F_{ry} \tag{6}$$

$$\frac{Dw}{Dt} - \frac{u^2 + v^2}{r} = -\frac{1}{\rho}\frac{\partial p}{\partial z} - g + 2\Omega u\cos\phi + F_{rz}.$$

These equations of motion are rather complicated, but can be simplified by applying scale analysis:

- the distance r can be replaced by Earth's radius a as the vertical distances from the Earth surface to air parcel are negligible comparing to the Earth's radius,

- the zonal wind is usually less than 100 m/s in magnitude: $(|u|\tan\phi)/a \ll 2\Omega\sin\phi$,

- vertical velocities w are usually much lower than horizontal velocities, while u and v are usually of a comparable magnitude:

$$|w\cos\phi| \ll |v\sin\phi|,$$

$$\frac{|wu|}{a} \ll 2\Omega|v\sin\phi|,$$

$$\frac{|wv|}{a} \ll 2\Omega|u\sin\phi|,$$

- the components $(u^2 + v^2)/a$ and $2\Omega u \cos\phi$ are very much smaller than g,

- the vertical component of the friction force F_{rz} is negligible.

With these simplifications we can rewrite equations of motion as:

$$\frac{Du}{Dt} = -\frac{1}{\rho}\frac{\partial p}{\partial x} + fv + F_{rx}$$

$$\frac{Dv}{Dt} = -\frac{1}{\rho}\frac{\partial p}{\partial y} - fu + F_{ry} \qquad (7)$$

$$\frac{Dw}{Dt} = -\frac{1}{\rho}\frac{\partial p}{\partial z} - g,$$

where $f = 2\Omega\sin\phi$ is Coriolis parameter. The equations are generally valid for synoptic motions, with an exception for synoptic motions near the equator [13], [14].

Thermodynamic equation

From the First Law of Thermodynamics the change in internal energy of a system equals to the difference between heat added to the system and work done by that system. The total thermodynamic energy in case of an air parcel is a sum of internal energy $\rho\delta V e$ and kinetic energy $\rho\delta V \frac{1}{2}\vec{u}\cdot\vec{u}$, where e is internal energy per unit mass.

External forces acting on the parcel are pressure force, gravity force and Coriolis force. The last one is always perpendicular to the direction of motion, adding no work to the system. Work done by the other two forces can thus be written as:

$$W = -\nabla\cdot(p\vec{u})\delta V - \rho\vec{g}\cdot\vec{u}\delta V.$$

The rate of diabatic heating, which represents the heating due to radiation, conduction and latent heat release can be written as $\rho\delta V J$, where J is diabatic heating per unit mass. The total change in internal energy of the parcel is then

$$\frac{D}{Dt}(\rho\delta V(e + \frac{1}{2}\vec{u}\cdot\vec{u})) = -\nabla\cdot(p\vec{u})\delta V - \rho\vec{g}\cdot\vec{u}\delta V + \rho\delta V J.$$

Left side of the equation can be expanded using the chain rule:

$$\frac{D}{Dt}(\rho\delta V(e + \frac{1}{2}\vec{u}\cdot\vec{u})) = \rho\delta V\frac{D}{Dt}(e + \frac{1}{2}\vec{u}\cdot\vec{u}) + (e + \frac{1}{2}\vec{u}\cdot\vec{u})\frac{D}{Dt}(\rho\delta V).$$

The second term on the right side of the equation equals to zero (continuity equation), while the first one can be rewritten by taking the dot product of $\vec{u}$ with the momentum equation $D\vec{u}/Dt = -2\vec{\Omega}\times\vec{u} - \frac{1}{\rho}\vec{\nabla}p + \vec{g}$ and neglecting the friction as

$$\rho\frac{D}{Dt}(\frac{1}{2}\vec{u}\cdot\vec{u}) = -\vec{u}\cdot\vec{\nabla}p - \rho w g.$$

Considering all the above the thermal energy balance is

$$\rho\frac{De}{Dt} = -p\vec{\nabla}\cdot\vec{u} + \rho J$$

or in more familiar form (taking into account $e = c_v T$ and $\frac{1}{\rho}\vec{\nabla}\cdot\vec{u} = -\frac{1}{\rho^2}\frac{D\rho}{Dt} = \frac{D\alpha}{Dt}$)

$$c_v\frac{DT}{Dt} + p\frac{D\alpha}{Dt} = J. \tag{8}$$

To get the final form of thermodynamic equation we define potential temperature:

$$\theta = T(\frac{p}{p_s})^{R/c_p}.$$

Applying the equation of state and using the relation $c_p = c_v + R$ the equation (8) becomes

$$c_p\frac{D\ln\theta}{Dt} = \frac{J}{T}.$$

After dividing potential temperature into basic state $\theta_0(z)$ and a deviation $\theta(x, y, z, t)$, the First Law of Thermodynamics for synoptic scale can be written as [15]:

$$\frac{1}{\theta_0}\left(\frac{\partial\theta}{\partial t} + u\frac{\partial\theta}{\partial x} + v\frac{\partial\theta}{\partial y}\right) + w\frac{d\ln\theta_0}{dz} = \frac{J}{c_p T}. \tag{9}$$

The basic equations form a system of non-linear partial equations which can be solved numerically for purposes of weather prediction. The most widely used numerical methods for solving the basic equations in weather forecasting models are finite difference method and spectral method. The first one uses the simple discretization where the derivatives of the variable are approximated by finite differences. In contrast to finite differences
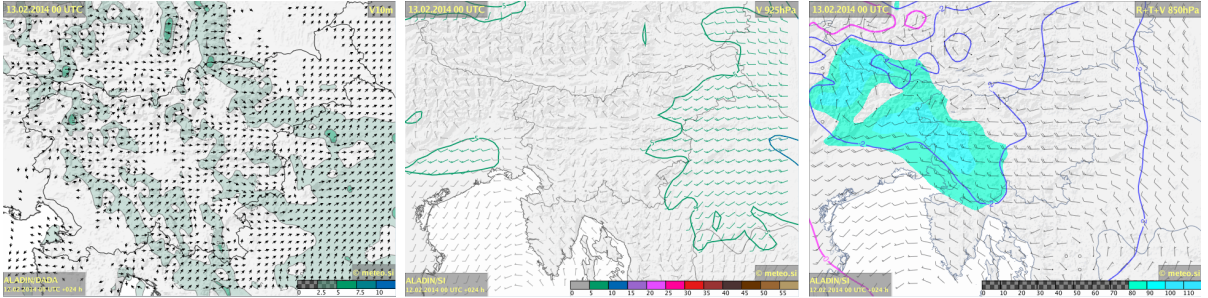

Figure 6: Forecasted wind fields at 10 m, 925 hPa and 850 hPa by meteorological spectral model ALADIN/SI [16].

the spectral method uses a finite series of orthogonal functions to represent the spatial variations. For global scale modeling with low resolution spectral method gives better results, while for better resolution the methods have comparable accuracy.

2.3 Analytic solution of the basic set of equations

Numerical solution is sometimes hard to interpret physically. In such a case analytical solution is needed to get a better understanding of the processes described by numerical solution. To obtain the analytical solution basic equations need to be linearized which can be done by using the pertutbation method. The perturbation method is a simple technique for quantitative analysis of the large-scale atmospheric motions, making it

possible to write the solution in a wave form. All variables (u, v, w, θ, p, ρ) are divided into a basic state part ($\bar{u}$, $\bar{v}$, $\bar{w}$, $\bar{\theta}$, $\bar{p}$, $\bar{\rho}$) and a perturbation part ($u^{'}$, $v^{'}$, $w^{'}$, $\theta^{'}$, $p^{'}$, $\rho^{'}$). The basic state part is assumed to be independent of time and longitude, while the perturbation part is a local deviation from the basic state part. In the theory, we assume that the basic state variables satisfy the basic equations, if perturbation part is equal to zero and the variables of perturbation part are small enough that their product can be neglected.

Inertia-gravity and topographic waves

In case of inertia-gravity waves, which are often named buoyancy waves, the effect of the Coriolis force on the air parcel can be neglected. The only two forces active in this case are buoyancy force in vertical and pressure gradient force. The movement of an air parcel in this case is a simple harmonic oscillation with frequency $\nu = N \cos \alpha$, where $N = g \, d \ln \theta_0 / dz$ is the buoyancy frequency and α is the angle between horizontal plane and the plane of movement of an air parcel. Basic set of equations in this case can be simplified to a 2-dimensional (2D) waves in x,z plane:

$$\frac{\partial u}{\partial t} + u \frac{\partial u}{\partial x} + w \frac{\partial u}{\partial z} + \frac{1}{\rho_0} \frac{\partial p}{\partial x} = 0$$

$$\frac{\partial w}{\partial t} + u \frac{\partial w}{\partial x} + w \frac{\partial w}{\partial z} + \frac{1}{\rho_0} \frac{\partial p}{\partial z} = 0 \qquad (10)$$

$$\frac{\partial u}{\partial x} + \frac{\partial w}{\partial z} = 0$$

$$\frac{\partial \theta}{\partial t} + u \frac{\partial \theta}{\partial x} + w \frac{\partial \theta}{\partial z} = 0$$

The atmosphere is considered to be incompressible, with density constant except where coupled with gravity in the vertical momentum equation (Boussinesq approximation). Linearizing the equations (10) using the perturbation method we get a simplified set of basic equations:

$$\left(\frac{\partial}{\partial t} + \bar{u} \frac{\partial}{\partial x} \right) u^{'} + \frac{1}{\rho_0} \frac{\partial p^{'}}{\partial x} = 0$$

$$\left(\frac{\partial}{\partial t} + \bar{u} \frac{\partial}{\partial x} \right) w^{'} + \frac{1}{\rho_0} \frac{\partial p^{'}}{\partial y} - \frac{\theta^{'}}{\bar{\theta}} g = 0 \qquad (11)$$

$$\frac{\partial u^{'}}{\partial x} + \frac{\partial w^{'}}{\partial z} = 0$$

$$\left(\frac{\partial}{\partial t} + \bar{u} \frac{\partial}{\partial x} \right) \theta^{'} + w^{'} \frac{d \bar{\theta}}{dz} = 0$$

After some basic mathematic operations and elimination of $\theta^{'}$ and $u^{'}$ the set of equations (11) yields a single equation for $w^{'}$:

$$\left(\frac{\partial}{\partial t} + \bar{u} \frac{\partial}{\partial x} \right)^2 \left(\frac{\partial^2 w^{'}}{\partial x^2} + \frac{\partial^2 w^{'}}{\partial z^2} \right) + N^2 \frac{\partial^2 w^{'}}{\partial x^2} = 0, \qquad (12)$$

13

which has a harmonic wave solution:

$$w' = \text{Re}\left[\hat{w}\exp(i\phi)\right] = w_r\cos\phi - w_i\sin\phi,$$

where $\phi = kx + mz - \nu t$. The horizontal wave number k has to be real due to a sinusoidal solution in x, while m can be either real (giving sinusoidal variations in vertical) or imaginary (giving exponential decay or growth in vertical).

Similar equation can be used to describe waves, which occur when air flows over a sinusoidal pattern of ridges. The waves in this case are stationary relative to the ground, w' is just a function of x and z:

$$\left(\frac{\partial^2 w'}{\partial x^2} + \frac{\partial^2 w'}{\partial z^2}\right) + \frac{N^2}{\bar{u}^2}w' = 0. \tag{13}$$

The solutions of the equation (13) are again dependent of m: $m = m_r$ gives vertically propagating waves with lines of constant phase tilted westward with hight (Fig. 7 left), while $m = m_i$ gives vertically decaying waves with no phase tilt (Fig. 7 right).
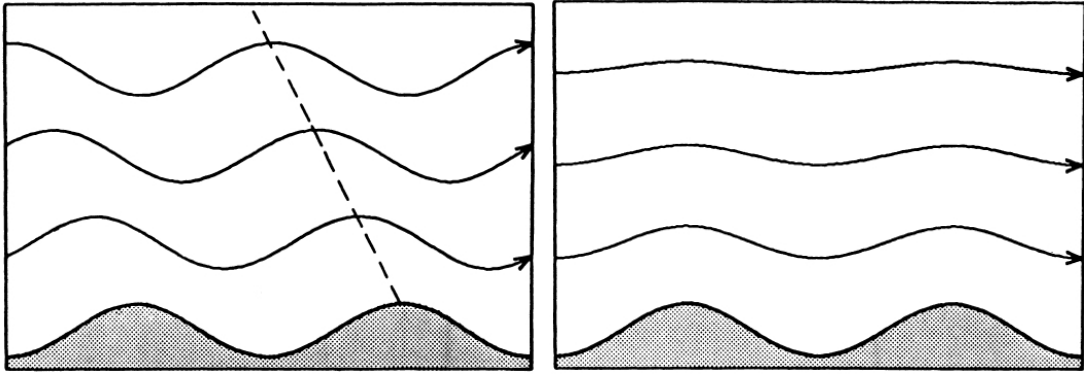

Figure 7: Topographic waves over sinusoidal pattern of ridges for two cases – $m = m_r$ (left) and $m = m_i$ (right). Figure taken from [15].

Mountain waves

Topographic features on Earth usually do not consist of sinusoidally repeating ridges, rather of isolated single ridges. To describe such a ridge the Fourier series can be used instead of a single harmonic function:

$$h_m(x) = \sum_{s=1}^{\infty} h_s\cos(k_s x),$$

where k_s is a wave number of a single mode. The total solution is a sum of contributions of either vertically propagating or vertically decaying single Fourier harmonics, depending on m being real or imaginary as before.

A special case of mountain waves are downslope windstorms. Their occurrence can be partly explained by the reflection of vertically propagating linear gravity waves in lower layer from the upper layer, which may produce enhanced surface winds, though not as

strong as being observed, which implies the nonlinear processes have to be taken into account as well. The flow can be characterized in three groups according to the Froude number (Fr), which determines the ratio between mean-flow speed and wave speed:

$$\mathrm{Fr}^2 = \frac{\bar{u}^2}{c^2}.$$

The flow is considered to be supercritical for Fr > 1, critical for Fr ≈ 1 and subcritical for Fr < 1. The behavior of the flow for supercritical and subcritical case is shown in Fig. 8a and 8b. In supercritical case the kinetic energy (KE) of the flow is converted to potential energy (PE) when the flow ascends the barrier, causing it to thicken and slow down while approaching the crest of the mountain and then accelerate at the lee side of the barrier as the potential energy is converted back to kinetic energy. In the subcritical case
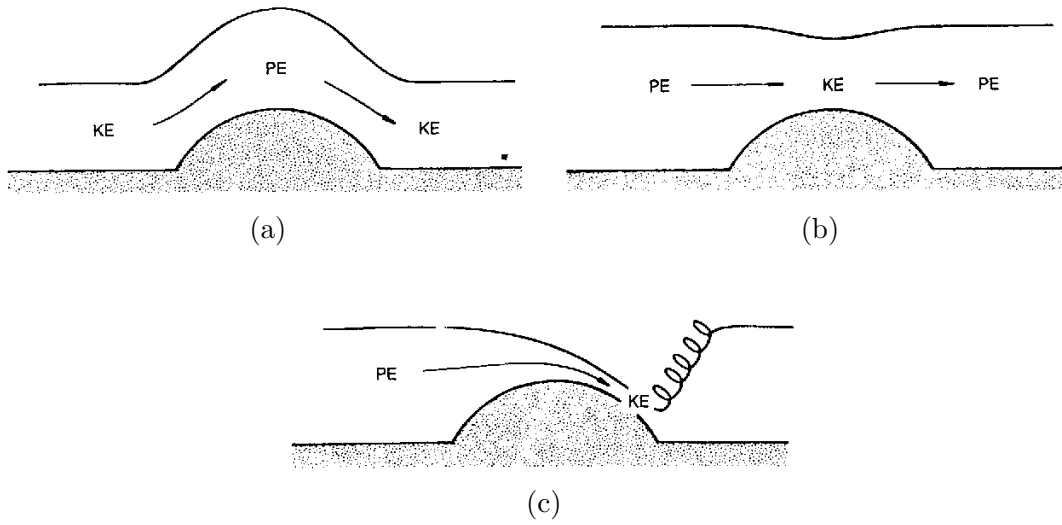

Figure 8: Subritical case (a), supercritical case (b) and the windstorm case (c). Figure taken from [15].

the flow accelerates while ascending the barrier, converting potential energy to kinetic energy at the crest of the barrier due to the drop in height of upper surface and then thickening again while descending, converting kinetic energy back to potential energy. The strongest winds are observed where both types of the flow are combined – the flow is subcritical while ascending the barrier, causing the air parcels to accelerate uphill, then converts to critical flow at the crest of the mountain and continues to supercritical flow down the lee side of the mountain, causing the already accelerated flow to gain even more speed, resulting in the strong lee side winds. The flow then experiences the hydraulic jump and adjusts back to ambient subcritical conditions (Fig. 8c) [15], [17]. The case of subcritical flow on the ascending and supercritical flow on the descending side of the barrier is referred to as the windstorm case and can be applied to the occurrence of the Bora wind.

3 Measurements of wind speed and direction

Measurements of atmospheric properties play an important role in the verification of meteorological models. In general, we can divide the measuring techniques in two groups: in-situ and remote sensing methods. In-situ measurements take part at or near the ground, using sensors which directly measure the properties of atmosphere, whether it is the temperature, pressure, humidity, wind speed and direction or any other observable. Remote sensing methods obtain the information of atmosphere properties by detection of a signal scattered on atmospheric features (clouds, aerosols, molecules). The observing technique can be based either on passive methods, where the scattering of natural radiation (i. e. sunlight) on objects is observed, or active methods, where system emits the signal and observes the return. In the scope of this seminar, only the techniques for wind field estimation will be presented.

Measurements of wind field have always presented a problem. Changes in wind speed and wind direction are often very abrupt, so the measurements are usually averaged over a period of time, typically over 15 - 60 minutes. Such measurements show general trend of wind speed, but provide no information about the wind speed maximum, so it is important to distinguish between wind speed and gust speed – first one represents the averaged value of wind over time, while the second one represents the maximum value in the given interval.

3.1 In-situ measurements

Traditionally, wind speed and direction measurements are made in-situ, providing the information on wind properties at the location of the measurements. A classic mechanical instrument for measuring the wind speed is a cup anemometer (Fig. 9a). Its advantages

(a) Cup anemometer.   (b) Hot-wire anemometer.   (c) Wind vane.
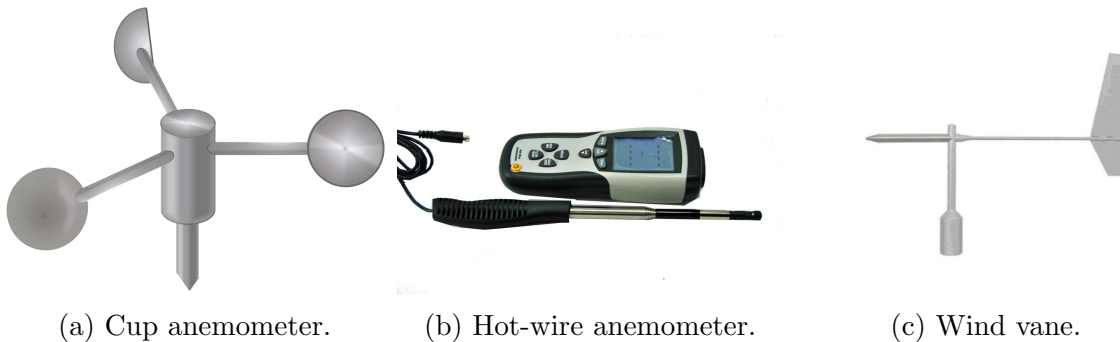
Figure 9: Different types of instruments for in-situ measurements of wind speed and direction.

are low cost and omni-directionality in horizontal plane, while its disadvantages are the starting threshold, making it unable to measure wind speeds under the threshold, and inertial effects, which results in smoothed wind speed curve and a phase lag. The propeller anemometer is a another type of mechanical instrument, where the main disadvantage is its directionality – it gives good response just for on-axis wind. Wind speed can be measured by non-mechanical instruments as well, for example by a hot-wire anemometer (Fig. 9b), which is a thermal instrument. It has the same problems as propeller

anemometer, but its advantage is fast response to changes in wind speed. In the case of cup and hot-wire anemometers, wind direction is determined using wind vanes. They usually consist of a horizontal arm with flat plate assembly on one side and a balanced counterweight on the other (Fig. 9c) [21]. A newer type of non-mechanical instrument is

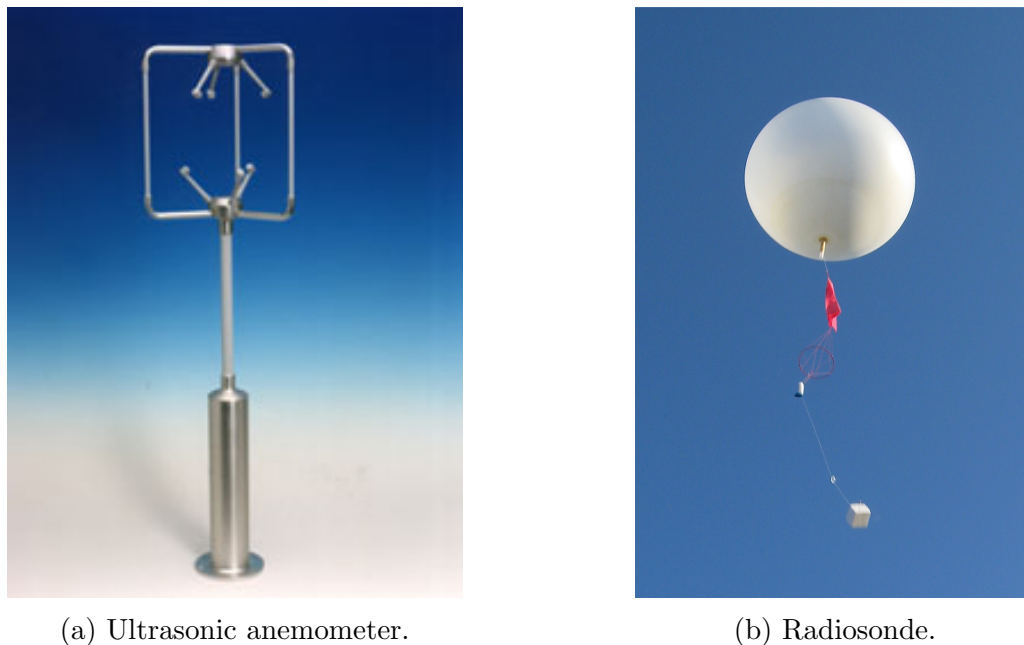(a) Ultrasonic anemometer.

(b) Radiosonde.

Figure 10: Different types of instruments for in-situ measurements of wind information. A radiosonde can provide a vertical profile of wind speed and direction.

the ultrasonic anemometer (Fig. 10a), which measures the wind speed based on time of flight of ultrasonic pulses between the pairs of transducers. Ultrasonic anemometer can measure either 2- or 3-dimensional wind vector with a fine temporal resolution (up to 50 Hz), which enables it to measure turbulence. Its main disadvantages are the distortion of the air flow due to the mechanical structure of the instrument and decreased accuracy in the case of precipitation. Anemometers are generally mounted on masts, enabling measurements at different levels close to the surface and reducing the effects of nearby objects (buildings, trees). Wind measurements higher in the atmosphere are conducted using radiosondes (Fig. 10b), where wind speed and direction can be obtained by tracking their position. Temporal and spatial resolution of radiosonde measurements is however rather poor (two radio soundings per day at very sparse locations, Fig. 11), as the number of launches per day is generally very limited. Limitations of the in-situ measurements are thus very localized information on the wind speed and the wind direction and poor temporal resolution in higher levels. Information about the 2-dimensional (2D) wind field can be obtained by a grid of anemometers extending over the entire region of interest, however, 3-dimensional (3D) wind field, usually needed to determine turbulence, remains out of reach.
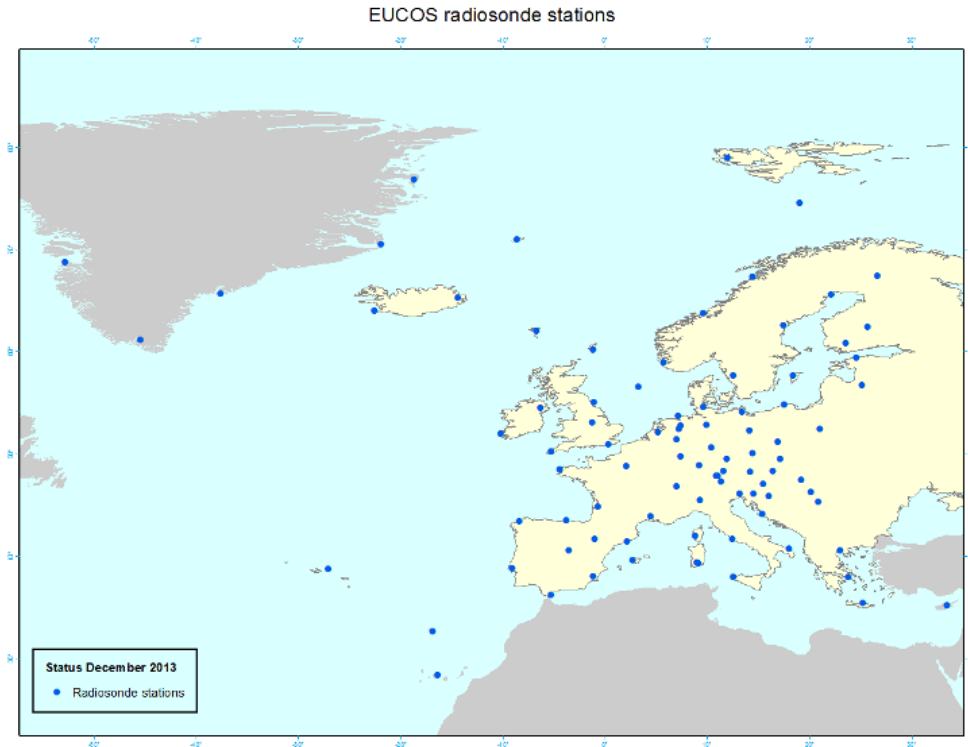
Figure 11: Locations of operative radiosonde stations in Europe in December 2013 [22]. The radiosonde stations closest to Vipava valley are Udine and Zagreb with two measurements per day and Ljubljana with one measurement per day.

3.2 Remote sensing

Remote sensing measurements are based on the detection of forward- or backscattered acoustic or electromagnetic signals. The advantage of these methods comparing to traditional ones is the ability to obtain 3D fields of observables as well as better spatial and temporal resolution of the data. Their main problem is the correlation between the measured signal and atmospheric properties, which are not related in a straight-forward fashion as in case of traditional in-situ measurements. According to the type of signals, we distinguish three types of remote sensing (RS) systems:

- SODAR (SOund Detecting And Ranging) – uses acoustic waves (wavelengths from 10 cm – 100 m),

- RADAR (RAdio Detecting And Ranging) – uses electromagnetic waves (wavelengths from 1 mm – 1 m),

- LIDAR (LIght Detecting And Ranging) – uses electromagnetic waves in UV and VIS range (wavelengths from 100 – 1000 nm).

Different signal wavelengths determine the structures that can be observed by the corresponding RS systems. SODAR systems detect the thermal inhomogeneities, RADAR systems the raindrops, while lidar systems detect small particles and molecules. The size of the detected structures defines the accuracy of the wind speed estimation – the
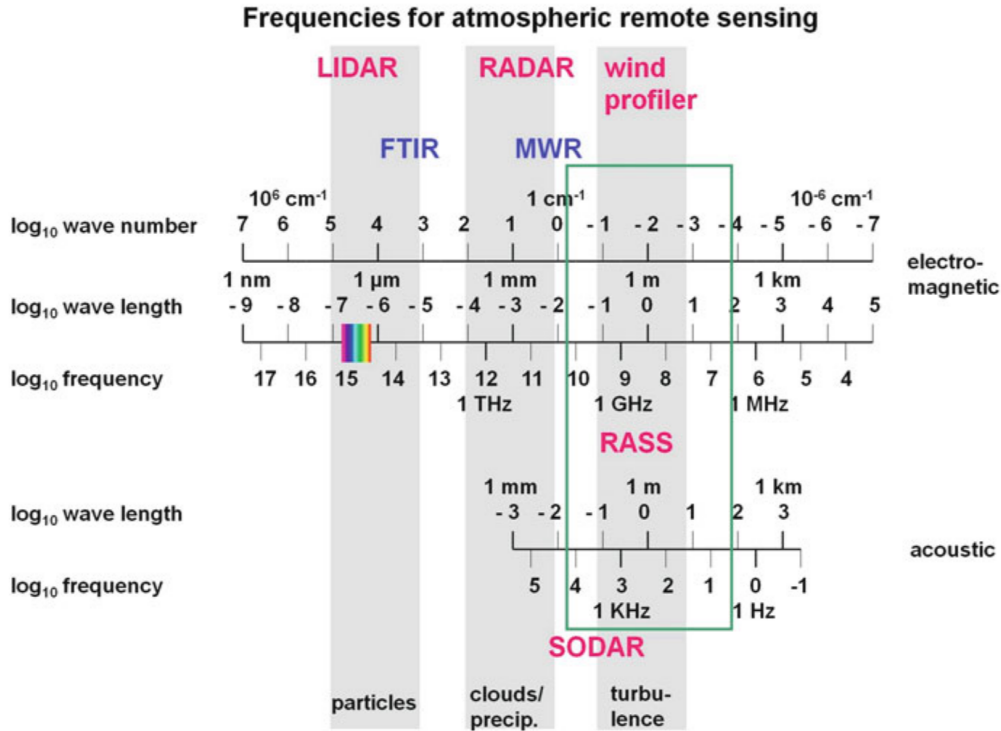
Figure 12: Wavelength ranges used by different RS systems and the atmospheric phenomena they can detect [23]. Lidar is the most appropriate system for wind field measurements as the observed structures are small enough it can be assumed they drift with the wind.

bigger the observed structures the less information of the wind speed we can obtain as the structures do not move with the wind.

3.2.1 Lidar measurements

Lidar measurements are based on the detection of light backscattered on molecules and aerosols in the air. A lidar device consists of a transmitter – strong light source capable of emitting short high energy pulses of light, and receiver – an optical system and photomultiplier collecting the backscattered light. The pulsed signal transmitted by the system is scattered in all directions by molecules and aerosols. Small portion of the signal is scattered back to the receiver, where the signal is analyzed to obtain wind speed. The distance between the observed structure and the transmitter is determined by the time delay between the emitted and the return signal. The return signal has to be corrected for the energy variation of the laser output and the inverse-range square decrease in signal [24]. Wavelengths used in lidar systems are from the UV, VIS and IR part of electromagnetic spectrum. The wavelength used depends on the type of scattering we would like to observe – the scattering on particles (Mie scattering) or on molecules (Rayleigh scattering). For the Rayleigh scattering the wavelengths of the electromagnetic radiation are much bigger than the size of observed molecules, while for Mie scattering the wavelengths are comparable to or greater than the size of the particles [25]. Mechanically, the transmitter - receiver configuration can either be bi-axial or co-axial. In bi-axial configu-
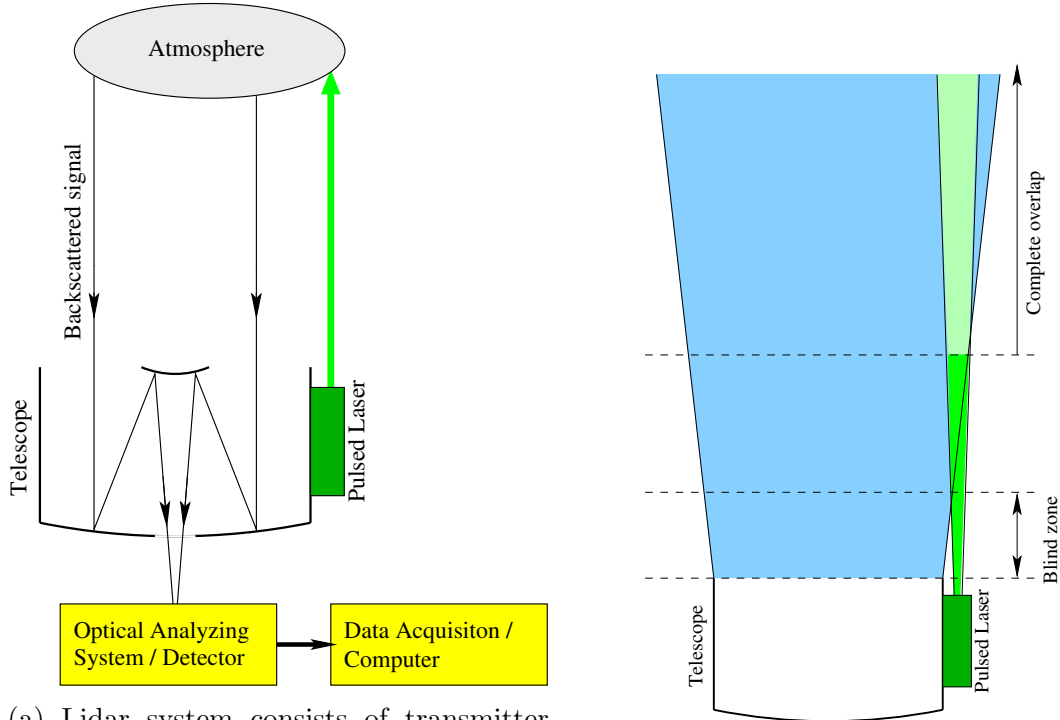
(a) Lidar system consists of transmitter (pulsed laser), receiver (telescope), detector (photomultiplier) and data aqusition system.

(b) Bi-axial configuration of lidar system. Blind zone is the region of no overlap in transmitter and receiver field of view.

Figure 13: Schematic setup of a lidar system and an example of bi-axial configuration of the transmitter and receiver.

ration the transmitter and receiver axis are separated, which results in a blind zone in the near range (Fig. 13b), while in co-axial configuration the axis of transmitter and receiver coincide, resulting in no blind zone in the near range. The advantage of the co-axial lidar is easier alignment of the transmitter and receiver axis, but the return signal of such a system often gets saturated in the near range. The bi-axial systems mostly work in full overlap region where the overlap function is well defined. Signal saturation does not occur due to blind zone in the near range.

For the purpose of wind field measurements two different configurations of lidar system can be used. The first one is a Doppler lidar, which uses scattering on molecules to measure the frequency shift of the return signal. The frequency shift determines the wind speed, while the direction of the largest frequency shift gives an information about wind direction. The second option for measuring wind speed with a lidar system is a rapid scanning elastic-backscatter lidar, where the wind speed and wind direction can be obtained from the drift of the aerosol structures. Both configurations use different scanning modes to obtain 3D wind field – plan position indicator (PPI) or velocity azimuth display (VAD) mode is used to obtain scan of the atmosphere at the constant elevation and different azimuth angles (Fig. 14a), while range height indicator (RHI) mode produces a scan at vertical plane (Fig. 14b).
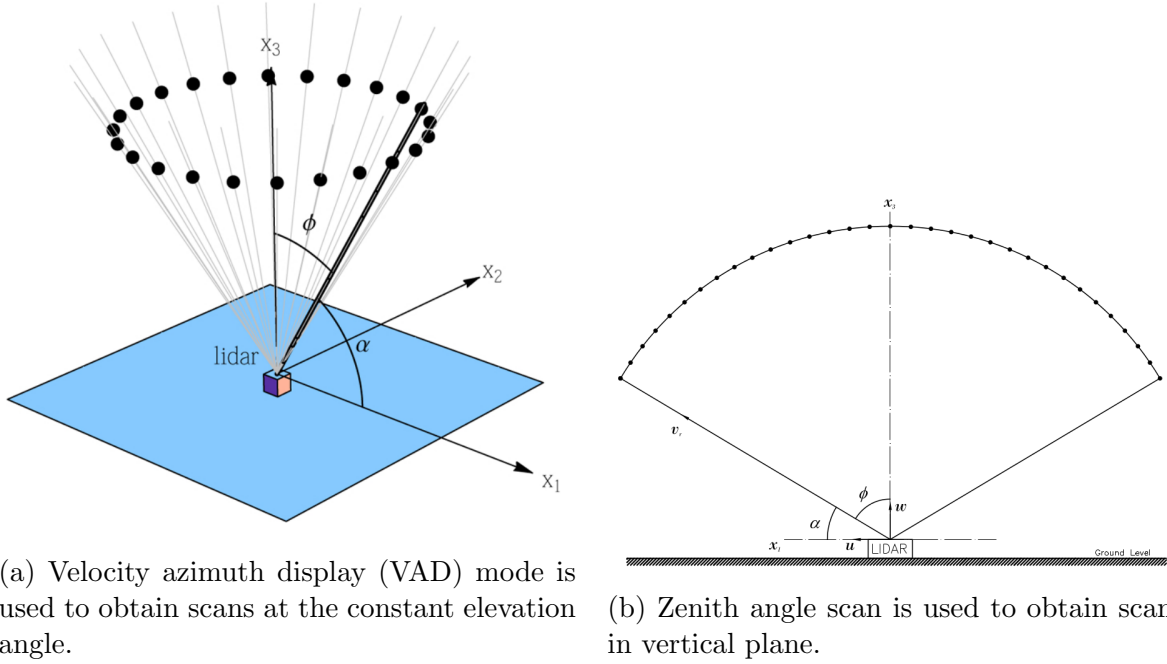
(a) Velocity azimuth display (VAD) mode is used to obtain scans at the constant elevation angle.

(b) Zenith angle scan is used to obtain scans in vertical plane.

Figure 14: Schematic of lidar operating in VAD and RHI scanning mode [26].

Doppler lidar system

Doppler lidar system evaluates the wind speed by measuring the Doppler shift of the backscattered signal. The radial component of wind (wind speed along the line of sight) can be obtained directly from the Doppler shift of the signal, while for 3D wind field the scanning at various azimuth angles is needed. The frequency of the returned signal can be evaluated using either coherent or direct (incoherent) detection. In the case of the
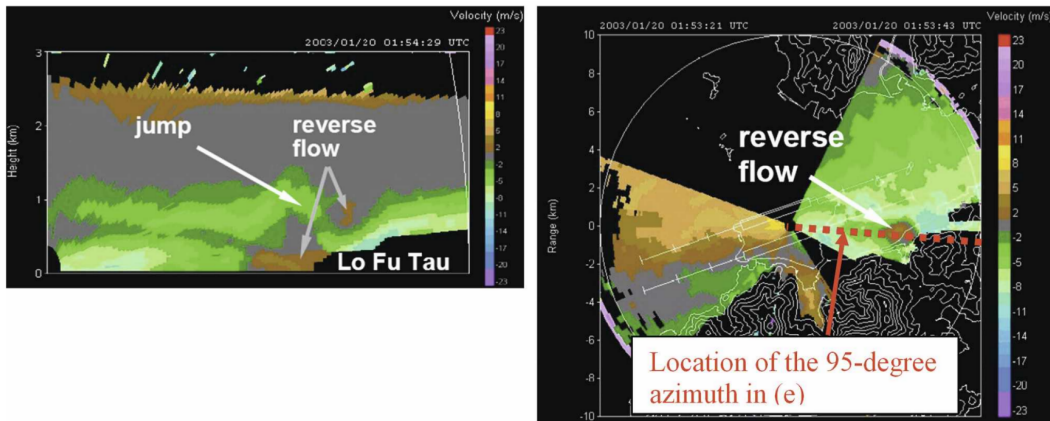

Figure 15: Vertical (left) and horizontal (right) wind field cross-section obtained by Doppler lidar [27]. The hydraulic jump at the seashore is clearly visible in both scans.

coherent detection, the system generates two signals with known offset in frequency. The primary signal is transmitted into the atmosphere, while the secondary signal is used as reference signal. The returned primary signal is optically mixed with the reference signal and sent to the detector, which measures the beat frequency between both signals

to determine the Doppler shift (heterodyne detection). In the case of direct detection, a few different techniques can be used to estimate the Doppler shift. Edge technique uses Fabry-Perot interferometer or an etalon as frequency to amplitude transducer and the frequency change is determined by the transmission change.

An example of measurements performed by a Doppler lidar is presented in [27]. Spatial resolution of the system used was 100 m in range from 400 m to 10 km with maximum detectable wind speed of 40 m/s. The lidar is capable of detecting the terrain-induced wind shear, hydraulic jumps and vortexes. The vertical and horizontal wind fields obtained from RHI and PPI scan respectively are presented in Fig. 15. In vertical scan the hydraulic jump and the reverse flow are clearly indicated.

Rapid scanning lidar system

In the case of the rapid scanning lidar, wind field information is obtained using correlation method, where aerosol features are identified and followed while drifting with the wind. The aerosols observed are small and light enough that it can be assumed they drift with the wind speed. The scanning lidar measurements are strongly dependent on the aerosol concentrations. In the case of low concentrations, problems due to weak return signal may arise, while in case of low clouds, fog or precipitation the return signal may be saturated or it does not contain the information about the wind speed, rather on the speed of the falling raindrops.
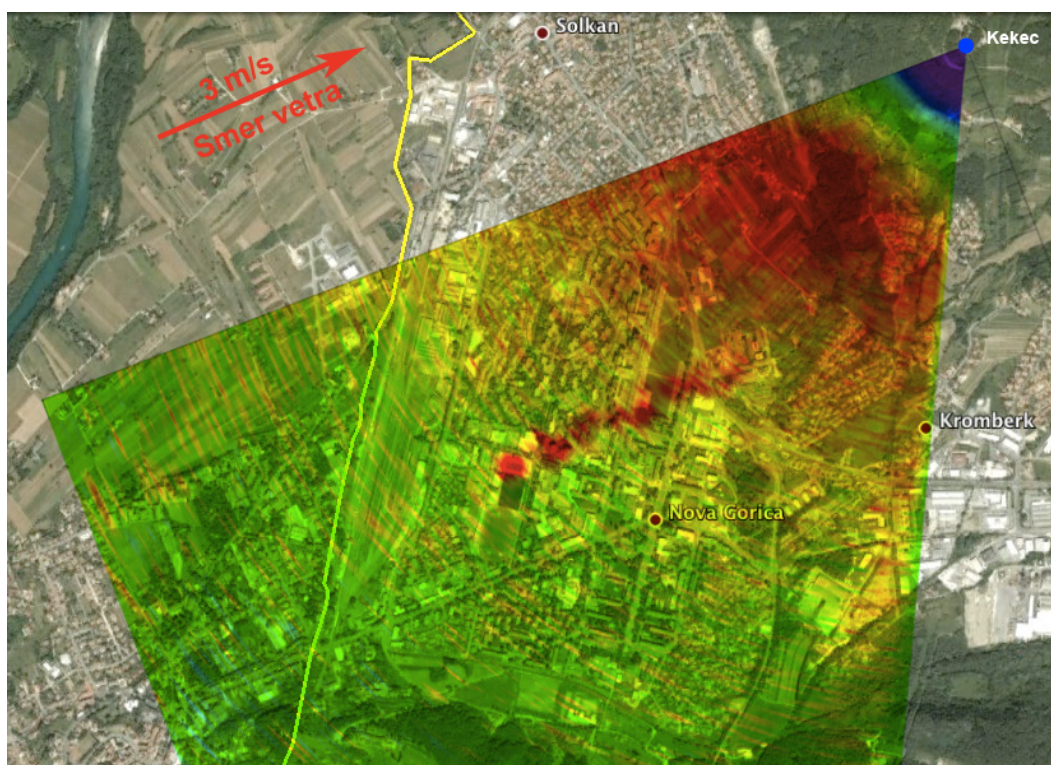

Figure 16: An example of horizontal scan of atmosphere by scanning elastic lidar of University of Nova Gorica [28]. The scan took about 5 minutes, which is too long for wind speed measurements but can give an idea about the wind direction.
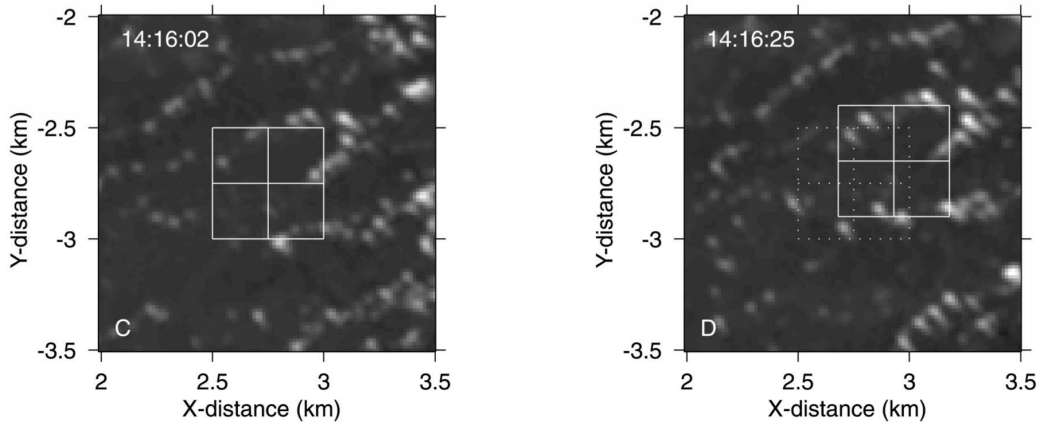
Figure 17: A section of two consecutive 90 ° PPI scans with fast scanning lidar system [29] used to obtain the wind field. The movement of aerosol structures in consecutive scans is marked with the full square.

An example of measurements of a 2D vector wind fields performed by a scanning lidar is presented in [29]. The scanning speed of the system for a 90 ° PPI scan was 3.75 °/s giving new scan every 24 s. The range of the system used was 18 km with resolution of 15 m. Fig. 17 shows a section of two consecutive PPI scans where the movement of aerosol structures can be seen. Lidar data was first corrected for inverse-range square decrease in return signal and the median high-pass filter was applied to eliminate large scale features. The data was then mapped in Cartesian system and the median of the desired field was computed. To remove the stationary features the median was subtracted from each scan. The resolution of obtained wind field was 250 m (Fig. 18).
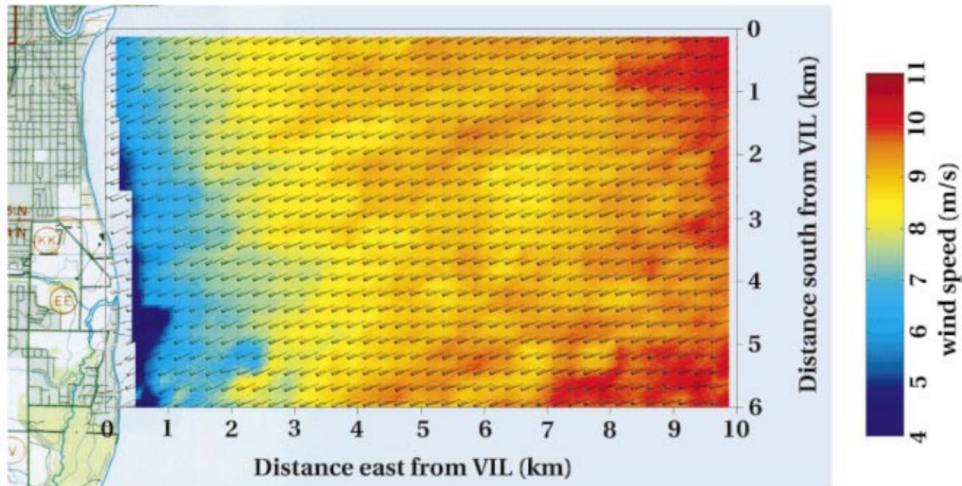

Figure 18: Wind field information derived from PPI scans with fast scanning lidar system [29]. The color shading is proportional to wind speed, while wind vectors in each point are represented by meteorological wind barbs with triangles indicating 5 m/s and a single barb indicating 1 m/s.

23

3.2.2 Satellite-based wind field measurements

Wind fields are being measured from satellites using either radar or lidar systems. One example of such a system is synthetic aperture radar (SAR). The SAR, which is a coherent side-looking radar system (Fig. 19), uses the flight path to simulate extremely large antenna, enabling it to measure atmospheric properties at a meter scale and obtaining high resolution imagery. The returns of the transmitted signal are collected for as long as the observed point is in the field of view of the radar beam and analyzed for the phase shift. Range-corrected returns are then coherently summed to yield the final information about the atmospheric properties.
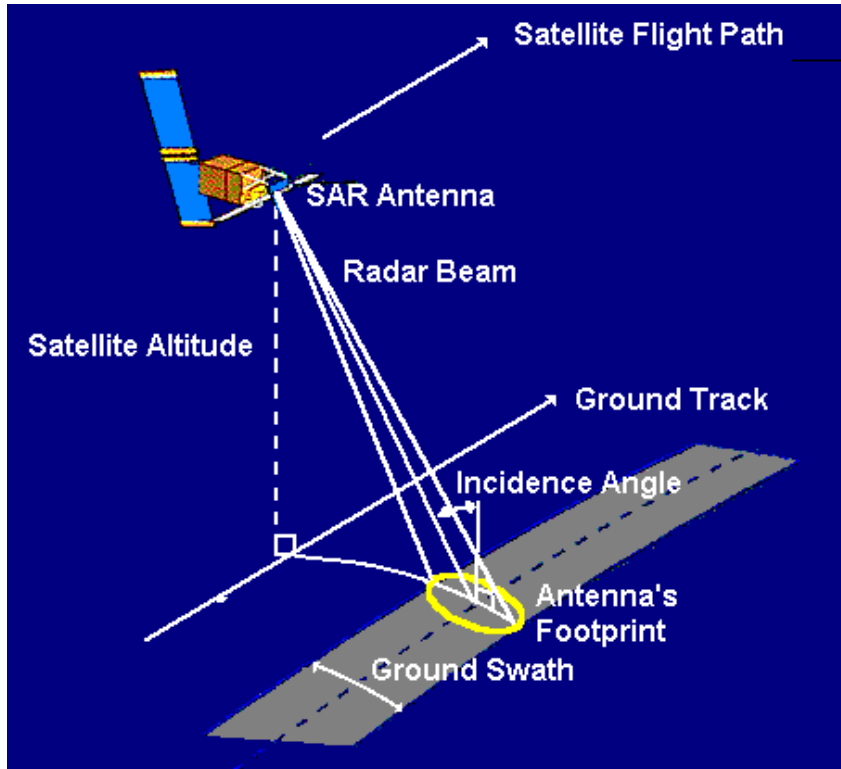

Figure 19: SAR system obtains information about atmospheric properties by collecting the returns of transmitted signal throughout the period in which the chosen target is in the field of view of the radar beam [30].

An example of wind field in the case of the Bora wind event acquired by Advanced SAR (ASAR) onboard the European Envisat satellite is presented in [31]. The wind field was observed indirectly through the sea surface roughness pattern. The obtained images enable observation of atmospheric gravity waves, wind jets, wakes and wave-induced rotors (Fig. 20a), while the actual wind field (Fig. 20b) is obtained by wind scatterometer model [31].
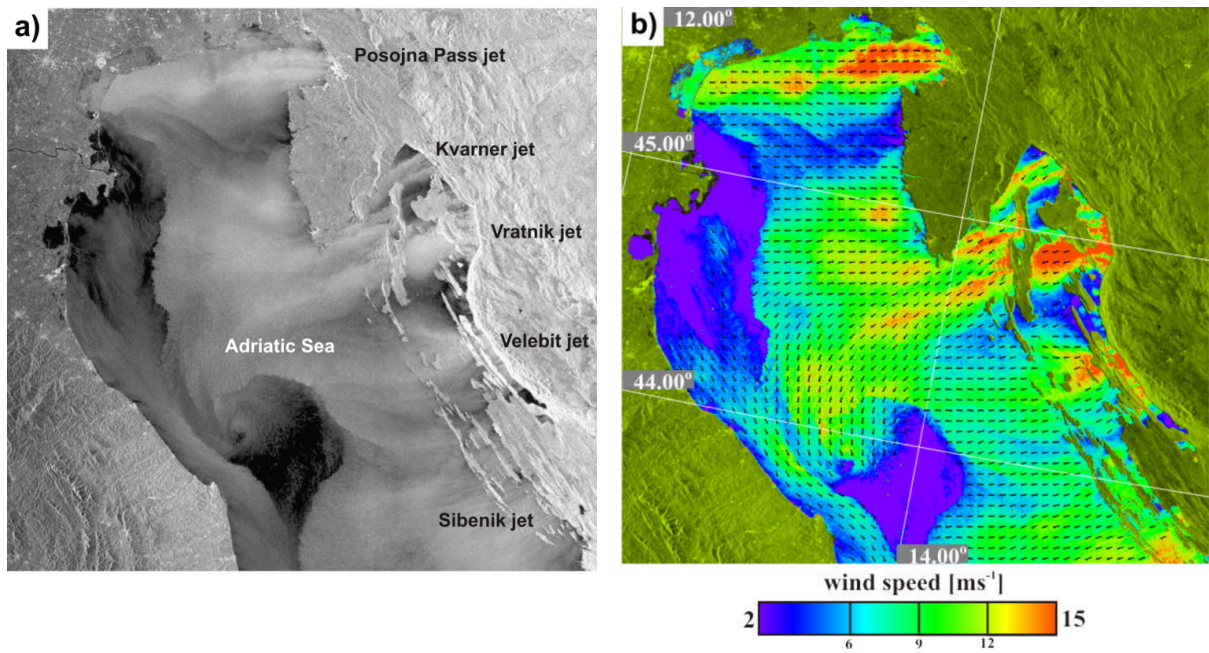
(a) The locations of jets related to the Bora wind event in N Adriatic region.

(b) The wind field of the Bora wind event obtained by the scatterometer model.

Figure 20: SAR image revealing the sea wave patterns caused by the Bora wind on 14 January 2006 (a). The corresponding wind field (b) was obtained by the scatterometer model [31].

4   Characterization of Bora wind in the Vipava valley

A case study of Bora wind events in the Vipava valley was performed for the period from 27 January to 24 April 2012, which was selected due to strong Bora wind outbursts at that time. The data sample[1] considered in this study includes wind and gust speed measured by 7 wind sensors, out of which 5 were dedicated cup anemometers, positioned 4 meters above the ground and arranged in the two lines perpendicular to the barrier, line A consisting of 3 and line B of 2 instruments (Fig. 21, coordinates of locations in Tab. 1a). The aim of positioning the sensors in lines perpendicular to the barrier was to
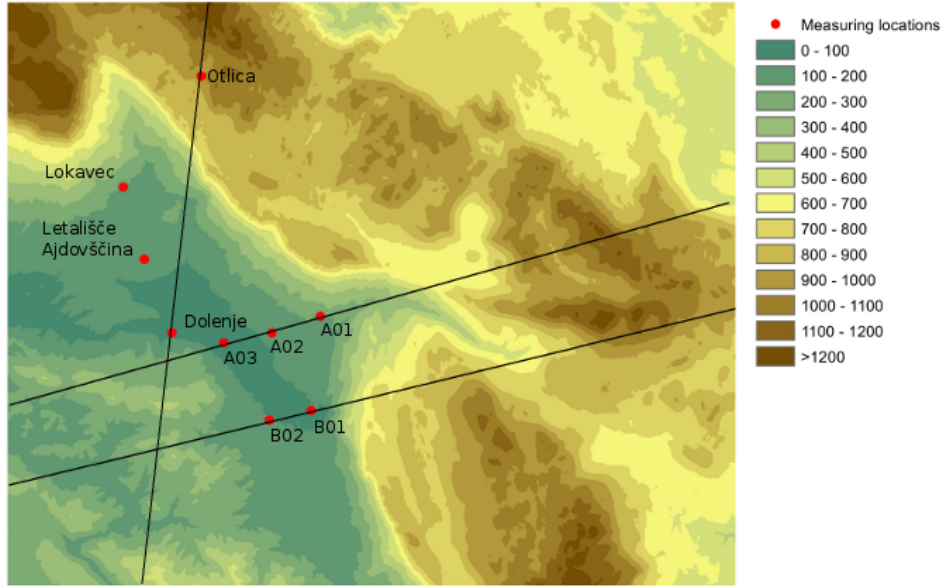

Figure 21: Orography of the part of Vipava valley with the locations of wind measurements. The lidar observatory of University of Nova Gorica at Otlica (upper left corrner) is located at GKX 88738 m, GKY 415972 m and elevation 945 m.

capture the downslope acceleration of the air-masses due to the steep terrain of the area – the altitude changes are from 300 m above see level (a.s.l.) high Karst plateau to 100 m a.s.l. Vipava valley and back to 1500 m a.s.l. high mountain barrier. The remaining two wind sensors are located at meteorological stations Otlica and Dolenje, the latter measuring the wind direction as well.

The measurements in lines A and B had a sampling rate of 10 seconds, measuring wind and gust speeds. In Tab. 2a some statistical properties of data are presented showing greater average values of wind speed ($\bar{v}$) for locations at lower altitudes (A02, A03, B02) compared to one on the slope of the mountain barrier (A01). Same can be said about maximum gust speed values, though the difference is smaller there (Tab. 2b). The comparison of hourly-mean wind speed for the first two episodes is presented in Fig. 23 on page 29, where the difference between measurements at different locations can be clearly seen. Throughout the episodes the hourly-mean wind speed exceeded the 3.3 m/s line (except for a short period in location B01) which is defined as the lower boundary for Bora

---

	X [m]	Y [m]	Z [m]
A01	81233	419663	214
A02	80809	418157	107
A03	80506	416678	89
B01	78403	419368	93
B02	78108	418083	105
Otlica	88738	415972	945
Dolenje	80820	415071	85

(a) Locations of wind measurements.

Episode	Beginning	End
1	27. 1. 2012 00:00 CET	8. 2. 2012 23:00 CET
2	9. 2. 2012 17:00 CET	13. 2. 2012 01:00 CET
3	20. 2. 2012 03:00 CET	23. 2. 2012 10:00 CET
4	26. 2. 2012 04:00 CET	26. 2. 2012 12:00 CET
5	3. 3. 2012 05:00 CET	7. 3. 2012 21:00 CET
6	8. 3. 2012 16:00 CET	11. 3. 2012 11:00 CET
7	1. 4. 2012 00:00 CET	1. 4. 2012 19:00 CET
8	8. 4. 2012 00:00 CET	9. 4. 2012 11:00 CET
9	14. 4. 2012 02:00 CET	14. 4. 2012 23:00 CET
10	16. 4. 2012 16:00 CET	18. 4. 2012 14:00 CET

(b) Bora events in period from 27 January to 24 April 2012.

Table 1: Locations of wind measurements in Gauss-Krüger coordinate system and the duration of bora wind events. A particular Bora event was determined by the general synoptic situation in the region and the wind direction at meteorological station Dolenje.
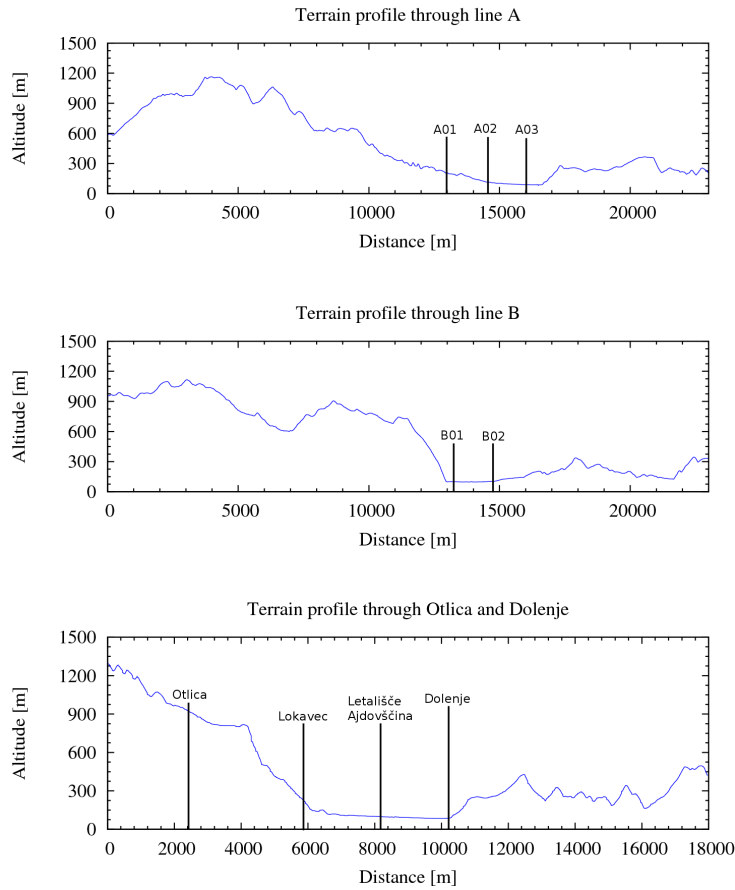

Figure 22: Terrain profiles through line A (top), line B (middle) and line Otlica - Dolenje (bottom).

wind events [32]. The lowest values of wind speed were measured at locations A01 and B01, which are located on the downslope side of the valley. The peaks of hourly-means coincide well as do the raises and falls in wind speed.

Episode	A01		A02		A03		B01		B02	
	$\bar{v}$ [m/s]	σ [m/s]	$\bar{v}$ [m/s]	σ [m/s]	$\bar{v}$ [m/s]	σ [m/s]	$\bar{v}$ [m/s]	σ [m/s]	$\bar{v}$ [m/s]	σ [m/s]
1	6.84	2.63	11.83	3.46	11.97	3.74	8.88	3.87	11.89	4.70
2	7.29	2.79	12.77	3.31	12.93	3.92	10.24	3.48	13.98	4.11
3	4.75	1.95	7.99	2.54	7.10	2.71	5.08	2.94	6.54	3.40
4	4.69	1.84	8.08	1.88	7.30	2.63	7.11	2.78	5.50	3.44
5	4.50	1.75	7.72	2.72	7.09	2.74	4.57	2.88	6.39	3.26
6	4.17	2.00	5.44	2.43	5.60	2.84	4.21	2.48	6.04	3.08
7	5.05	2.75	7.64	4.12	7.70	4.46	6.74	4.59	6.20	4.08
8	2.99	2.03	4.16	2.56	4.37	2.55	3.32	2.81	2.64	2.13
9	2.89	1.47	6.21	1.73	/	/	4.64	1.89	5.76	2.59
10	3.54	1.79	5.53	2.07	5.34	2.18	4.27	2.78	4.35	2.36

(a) Average values and standard deviations of wind speed at locations in line A and B for selected Bora wind events.

Episode	A01	A02	A03	B01	B02
	v_{max} [m/s]	v_{max} [m/s]	v_{max} [m/s]	v_{max} [m/s]	v_{max} [m/s]
1	25.13	28.93	30.07	30.45	33.5
2	27.79	33.88	36.17	31.22	33.88
3	16.75	19.41	20.18	22.84	27.03
4	14.47	19.41	22.84	21.7	19.03
5	17.89	21.32	22.84	20.18	23.22
6	15.99	16.37	17.13	18.65	20.56
7	20.18	22.08	24.36	23.98	22.84
8	12.94	14.85	15.23	17.13	15.61
9	11.04	13.7	/	15.23	16.37
10	13.7	20.18	19.8	21.7	15.61

(b) Maximum gust speeds at locations in line A and B for selected Bora wind events.

Episode	Otlica			Dolenje		
	$\bar{v}$ [m/s]	σ [m/s]	v_{max} [m/s]	$\bar{v}$ [m/s]	σ [m/s]	v_{max} [m/s]
1	4.8	1.9	18.5	3.1	1.0	16.5
2	9.8	3.2	35.4	7.4	2.6	30.0
3	11.2	1.3	32.1	8.2	2.9	35.9
4	6.2	2.2	24.6	4.9	1.4	21.1
5	5.2	1.6	15.8	4.2	2.0	16.7
6	5.0	2.4	21.2	4.7	1.6	20.6
7	6.6	1.9	22.9	3.9	1.4	14.9
8	5.6	3.1	22.9	4.0	2.5	17.1
9	4.4	1.4	16.4	2.9	0.9	13.4
10	7.5	0.8	19.4	4.0	0.9	16.2

(c) Average values and standard deviations of wind speed and maximum gust speeds at meteorological stations Otlica and Dolenje for selected Bora wind events.

Table 2: Average value $\bar{v} = \frac{1}{N} \sum v_i$ and standard deviation $\sigma = \sqrt{\frac{1}{(N-1)} \sum (v_i - \bar{v})^2}$ of wind speed and maximum values of gust speed for both lines and for the meteorological stations Otlica and Dolenje. Sampling rate is 10 seconds at locations in lines A and B, and 30 minutes at Otlica and Dolenje. The downslope acceleration is clearly visible in average wind speeds obtained at different locations as well as in maximum values of gust speeds for both lines. The location of meteorological station Dolenje is not optimal for Bora wind measurements due to the proximity of obstacles. Although the location A03 is positioned nearby (Fig. 21), the differences in the obtained maximum gust speed values at these two locations are evident (Tab. 2b for A03 and Tab. 2c for Dolenje).
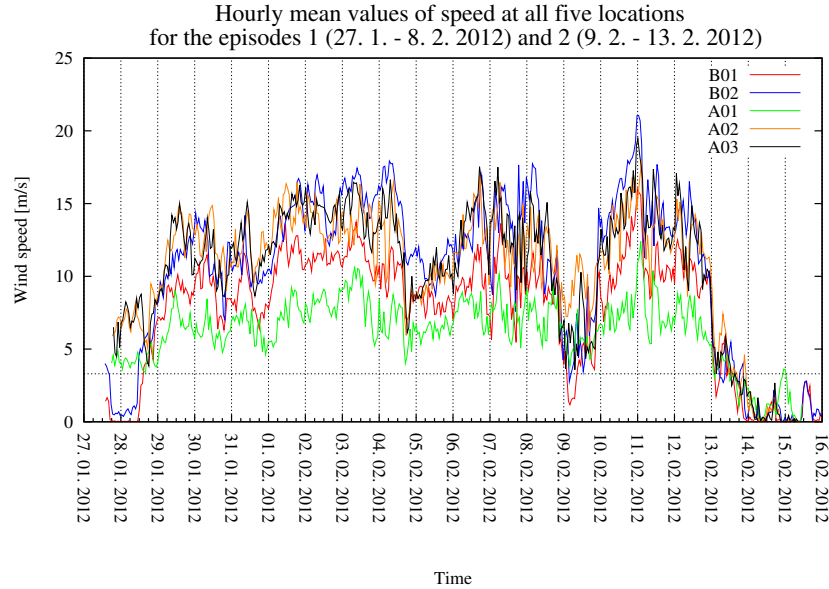
Figure 23: The hourly-mean wind speed at all five locations for the Episodes 1 (27. 1. - 8. 2. 2012) and 2 (9. 2. - 13. 2. 2012). The horizontal dashed line represents the lower level of the wind speed (3.3 m/s) at which the wind can still be characterized as Bora. The difference in wind speed between locations A01 and A02, A03 is clearly visible with wind speeds occasionally reaching double values at later two. The difference in wind speed for line B is not as large, but still visible.

The obtained data set was subject to Fourier transform analysis to uncover possible periodicity of wind gusts. Frequency spectra for Episode 1 data taken at all measuring locations (Tab. 1a) are shown in Fig. 24. No single evident frequency peak was observed, which is in agreement with known Bora wind gust properties. Wind gusts usually build up and decay quite fast, while the period of time between two consecutive gusts can be
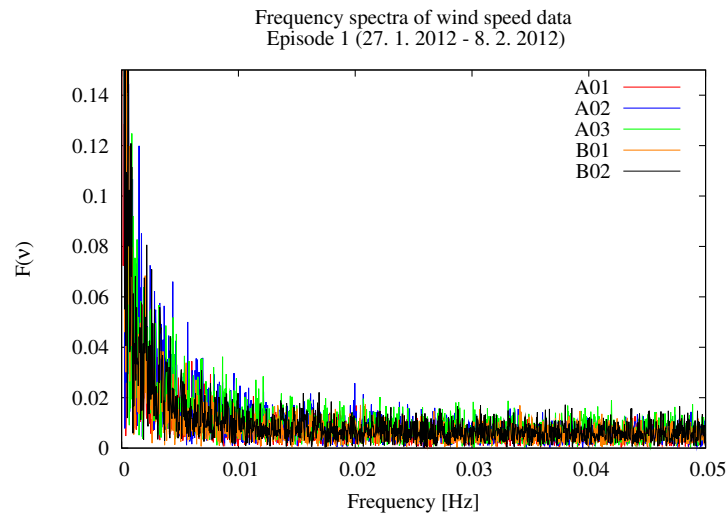

Figure 24: The frequency spectra of the wind speed data for the Episode 1 (27. 1. - 8. 2. 2012) for all five measuring locations.
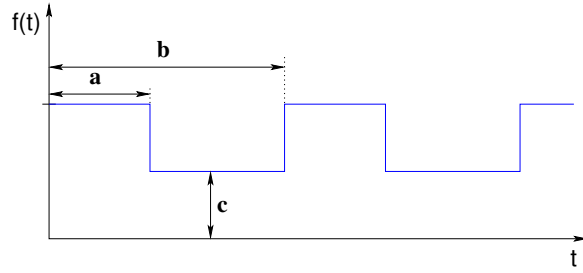
29

Figure 25: Pulse wave with pulse duration a, period b and a baseline c was used as an approximation of wind gusts.

characterized as constant air flow with an averaged wind speed. As a fist approximation of the gusts we considered a pulse wave with pulse duration a, period b and a baseline c (Fig. 25). A Fourier transform of a pulse wave yields

$$f(t) = \frac{\tau}{T} + \sum_{n=1}^{\infty} \frac{2}{n\pi} \sin\left(\frac{\pi na}{b}\right) \cos\left(\frac{2\pi n}{b}t\right)$$

which means that the period defines frequency peaks while the duration sets their relative amplitudes. Visual comparison of the pulse wave spectrum with periods close to 6 minutes and durations around 80 seconds seem to approximate the peaks in frequency spectrum of wind speed data quite well (Fig. 26), although a detailed maximum likelihood analysis remains to be performed to optimize the pulse wave parameters. In addition, the possibility of a superposition of several waves will need be explored and a more realistic wind gust shape will need to be determined.
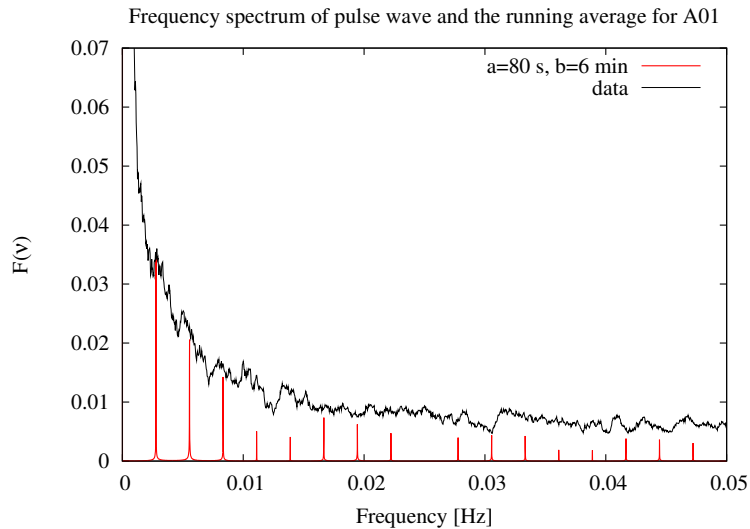

Figure 26: Comparison of the frequency spectrum of the wave pulse and the running average over 210 seconds of the frequency spectrum of the wind speed at location A01 for Episode 1. The amplitude of the pulse wave frequency spectrum was scaled to match the amplitude of the peak at approximately 0.003 Hz in the wind speed data for easier visual comparison.

In-situ wind measurements can not describe all the relevant processes taking place in the desired area by themselves. A better overview of those processes is generally obtained by numerical models, using the in-situ wind measurements as the basis for the estimation of initial and boundary conditions, as well as for the verification of the information obtained by the simulations. To fully verify 3D wind field model results, in-situ measurements are not suitable as they can not provide the desired 3D wind field data with sufficient spatial and temporal resolution. This type of information can be obtained by the use of a lidar system, which can obtain the wind field data with spatial resolution of a few meters and temporal resolution of a few seconds. There are several requirements such a system has to meet – it has to be small enough to allow the mobility needed to measure wind profiles at various locations in complex terrain configuration, it has to be able to scan in two directions (zenith and azimuth angle) and it has to scan the desired area fast enough to be able to trace the movements of aerosols and other structures in the atmosphere. The need for fast scanning introduces the need of a fast data acquisition system, which has to be able to capture and process large amounts of data in very short time.
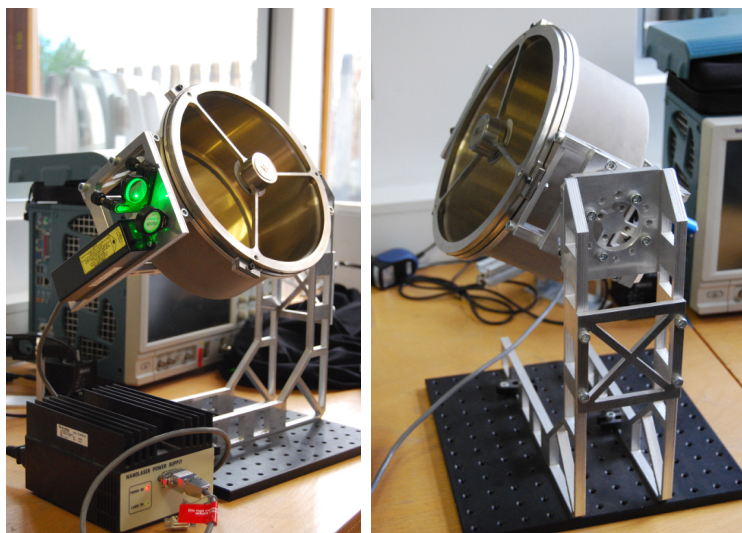

Figure 27: A small rapid scanning lidar system in development. The system will use green light laser (532 nm) with high repetition rate as a transmitter and custom made electronics for data acquisition.

A small rapid scanning lidar system is currently being developed at University of Nova Gorica (Fig. 27). It consists of a receiver (Ritchey-Crétien optic system with two hyperbolic mirrors) mounted onto a support frame enabling movements in alt-azimuthal direction, and a transmitter – Nd:YAG pulsed laser (532 nm, 5 kHz repetition rate, energy 3 μJ/pulse). Light return will be collected by a photomultiplier tube, followed by the custom made electronics for fast data acquisition. The transmitter and receiver are bi-axial, which results in a blind region in near range. For the purposes of aerosol tracing full overlap is not required,so the system is expected to operate within a range of 10 to 500 m at scanning speed of 10 °/s. The use of the correlation technique is possible if aerosol structures stay in the scanned field for at least two consecutive scans (Fig. 17), which limits the maximum observable speed to approximately 40 m/s in direction perpendicular

to the laser beam. As Bora wind flows are expected to be vertically relatively narrow and close to the ground, such a device should be able to provide the depth of the Bora wind layer in either fixed or scanning mode and a 2D wind field profile in zenith angle scanning mode, such as for example in Fig. 18.

5 Conclusions

Bora wind phenomenon has been extensively studied in the past using a variety of different experimental techniques (in-situ measurements, synthetic aperture radar (SAR), sodar, etc.), as well as modeled with a number of different numerical models (fluid mechanics, hydrostatic, meteorological models). Some characteristics of Bora wind events remain as yet unclear, such as the development of strong wind gusts, the frequency and eventual periodicity of the gusts as well as the 3D structure of the Bora wind flow. The presented case study, using wind speed data collected by cup anemometers at 10 s sampling rate, has shown limitations of this data regarding the periodicity of the gusts, which is limited to occurrences above 20 seconds, as well as regarding the shape of the gusts. Both information, crucial for the construction of a wind gust model that will adequately describe the data, will become available using modern instrumentation. Ultrasonic anemometers, which enable the retrieval of wind information at frequencies up to 50 Hz and are capable of wind vector measurements, will be used as they will offer a better insight into the wind gust shape and periodicity. Denser wind vector data is expected, in combination with advanced analysis techniques (wavelets, recurrence plots, etc.), to advance the present understanding of the Bora wind gust properties. Additional progress is expected to be made using wind profiles obtainable by a fast scanning elastic lidar, yielding depth of the Bora wind flow and 2D wind fields.

6 Acknowledgments

References

[1] http://www.treehouse-maps.com/, 12. 2. 2014.

[2] Petkovšek, Z., 2004: Burja v Sloveniji in nekoliko južneje. *Pol stoletja Slovenskega meteo-rološkega društva.* Ljubljana: Slovensko meteorološko društvo, 251-268.

[3] Žagar, M., Rakovec, J., 2007: Characteristics of the Bora wind under different conditions of the lee background flow. *29*[th] *International Conference on Alpine Meteorology ICAM 2007, Extended Abstracts*, vol. 2, 309-312.

[4] www.tic-ajdovscina.si, 4. 11. 2013.

[5] www.siol.net, 4. 11. 2013.

[6] www.24ur.com, 4. 11. 2013.

[7] Paradiž, B., 1957: Burja v Sloveniji. *10-let Hidrometeorološke službe SRS.* Ljubljana: Hidrometeorološki zavod LR Slovenije, 147–172.

[8] Yoshino, M. M., 1976: Local wind Bora: A research summary. *Local wind Bora.* University of Tokio Press, 277-282.

[9] Menezes, A., Tabeaud, M., 2000: Variations in Bora weather type in the north Adriatic See, 1866 - 1998. *Weather*, vol. 55, 2000, 452-458. University Press

[10] Petkovšek, Z., 1976: Periodičnost sunkov burje. *Razprave*, vol. 20, no. 2, 1976, 67-75.

[11] Jeromel, M., Malačič, V., Rakovec, J., 2009: Weibull distribution of Bora and sirocco winds in the northern Adriatic Sea. *Geofizika*, vol. 26, no.1, 2009, 85-100.

[12] www.nawindpower.com/issues/NAW1301/FEAT_06_Why_Atmospheric.html, 25. 11. 2013.

[13] Fleagle, R. G., Businger, J. A., 1980: *An Introduction to Atmospheric Physics.* New York: Academic Press, Inc.

[14] Andrews, D. G., 2010: *An Introduction to Atmospheric Physics, Second Edition.* New York: Cambridge University Press.

[15] Holton, J. R., 2004: *An Introduction to Dynamic Meteorology, Fourth Edition.* Oxford: Elsevier Academic Press.

[16] http://meteo.arso.gov.si/, 12. 2. 2014.

[17] Durran, D. R., 2002: Downslope winds. *Encyclopedia of Atmospheric Sciencies*, Elsevier Science Ltd., 2003, 644 - 650.

[18] http://www.logotronic.at, 7. 1. 2014.

[19] http://www.geographylwc.org.uk/GCSE/igcse/weather/images/anemometer.gif, 7. 1. 2014.

[20] http://radiosondemuseum.org, 7. 1. 2014.

[21] 1992: Meteorological measurements guide. New Mexico: Secretariat Range Commanders Council.

[22] http://www.eumetnet.eu/, 20. 2. 2014.

[23] Emeis, S., 2011: *Surface-Based Remote Sensing of the Atmospheric Boundary Layer.* London: Springer.

[24] Hooper, W. P., Eloranta, E. W., 1985: Lidar Measurements of Wind in the Planetary Boundary Layer: The Method, Accuracy and Results from Joint Measurements with Radiosonde and Kytoon. *Journal of Climate and Applied Meteorology*, vol. 25, July 1986, 990 - 1001.

[25] Gao., F., 2012: *Study of Processes in Atmospheric Boundary Layer over Land-Sea Transition Interface Using Scanning Lidar. Dissertation.* Nova Gorica.

[26] Sathe, A., Mann, J., 2013: A review of turbulence measurements using ground-based wind lidars. *Atmospheric Measurement Techniques Discussions*, vol. 6, no. 4, 2013, 6815 - 6871.

[27] Shun, C. M., Chan, P. W., 2007: Applications of an Infrared Doppler Lidar in Detection of Wind Shear. *Journal of Atmospheric and Oceanic Technology*, vol. 25, May 2008, 637 - 655.

[28] He, T.-Y., Stanič, S., Gao, F., Bergant, K., Veberič, D., Song, X.-Q., and Dolžan, A, 2012: Tracking of urban aerosols using combined LIDAR-based remote sensing and ground-based measurements. *Atmospheric Measuring Techniques*, vol. 5, 2012, 891 - 900.

[29] Mayor, S. D., Eloranta, E. W., 2001: Two-Dimensional Vector Wind Fields from Volume Imaging Lidar Data. *Journal of Applied Meteorology*, vol. 40, August 2001, 1331 - 1346.

[30] http://www.crisp.nus.edu.sg, 12. 3. 2014.

[31] Alpers, W., Ivanov, A., Horstmann, J., 2008: Observations of Bora Events over Adriatic Sea and Black Sea by Spaceborne Synthetic Aperture Radar. *Monthly Weather Review*, vol. 137, March 2009, 1150 - 1161.

[32] Pristov, N., Petkovšek, Z., Zaveršek, J., 1989: Some characteristics of bora and its beginnings in Slovenia. *Razprave*, vol. 30, no. 1, 1989, 37-52.